RESEARCH

Low-temperature flash sintering of dense Ta-doped $Li_7La_3Zr_2O_{12}$ solid electrolyte for solid-state lithium batteries

Yue Yang[1] · Zheng Zhang[1] · Tianhui Ma[1] · Shaoting Jia[1] · Chao Huang[1]

Abstract

To achieve high density and high Li-ion conductivity in the garnet LLZO ($Li_7La_3Zr_2O_{12}$), an effective strategy is to dope it with high-valence elements to stabilize the cubic phase and to lower the sintering temperature. As well known, flash sintering (FS) is characterized by short sintering times and low furnace temperature. Herein, the doping modification of Ta-LLZO by flash sintering at 700 °C for the higher conductivity of LLZO was investigated in the present study. The results indicate that the addition of an appropriate amount of Ta^{5+} can enhance the ionic conductivity. The relative density of the sintered cubic $Li_{6.4}La_3Zr_{1.4}Ta_{0.6}O_{12}$ is 94.72%, with a corresponding total ion conductivity of 9.8×10^{-4} S cm^{-1}, demonstrating good electrical performance. A solid-state lithium metal battery with $Li_{6.4}La_3Zr_{1.4}Ta_{0.6}O_{12}$ electrolyte was assembled, and its electrical performance was tested at 50 °C. The results showed that an initial discharge specific capacity of 126.5 mAh g^{-1} at a 0.1C rate could be reached.

Keywords Flash sintering · Solid-state electrolyte · Ta-LLZO · Lithium metal batteries

Introduction

With the widespread use of portable electronic devices and the rapid growth of electric vehicles, there has been an increasing demand for lithium-ion batteries (LIBs). Traditional LIBs, which use liquid electrolytes, are prone to leakage and flammability, posing safety hazards such as fire and explosions [1–4]. Therefore, the all-solid-state lithium batteries (ASSLBs), composed of a reliable thermally stable solid-state electrolyte and a lithium metal anode with ultrahigh specific capacity and the lowest reduction potential, are considered the most promising alternative products. As a key part of ASSLBs, solid electrolyte preparation has been proposed and received increasing attention in recent years [5, 6].

Among various types of solid electrolyte materials, garnet oxide $Li_7La_3Zr_2O_{12}$ and its chemical derivatives have

attracted significant attention due to their excellent room temperature conductivity, wider electrochemical stability window, and their electrochemical stability towards lithium metal [7–10]. They are considered one of the candidate materials for the next-generation solid electrolytes in solid-state lithium-ion batteries, with promising prospects for a wide range of applications. The phase structure of LLZO is particularly important for its performance, and it can be divided into the cubic phase LLZO (c-LLZO) and the tetragonal phase LLZO (t-LLZO). In particular, the cubic phase LLZO exhibits a 2–3 order of magnitude higher room temperature conductivity compared to the tetragonal phase [8, 11, 12]. However, the formation of the ideal cubic phase of LLZO relies on element doping [13–15]. In this regard, LLZO doped with Ta seems to be attractive as it exhibits high lithium-ion conductivity and good chemical stability towards electrode materials [16–18].

Sintering of LLZO is a key factor determining its performance, including density, conductivity, and critical current density. In the conventional solid-state sintering [19–22] of LLZO, solid electrolyte requires sintering at high temperatures (> 1000 °C) for several hours or even tens of hours to achieve higher densification and sufficient ionic conductivity. When the sintering temperature is maintained at a high state for an extended duration, lithium loss will occur, leading to a

✉ Yue Yang
  yangyue@ccut.edu.cn

[1] Key Laboratory of Advanced Structural Materials,
  Ministry of Education & Advanced Institute of Materials
  Science, and School of Materials Science and Engineering,
  Changchun University of Technology, Changchun 130012,
  China

decrease in ionic conductivity. To offset the loss of lithium, most LLZO briquettes are packaged in "mother powder" during the sintering process to reduce lithium loss. However, the use of this green powder results in higher processing costs. Inada et al. [19] prepared tantalum-doped LLZO using the solid-state sintering method at 1200 °C for 24 h achieving an electrical conductivity of 6.1×10^{-4} S cm^{-1}. Huang et al. [22] employed the traditional solid-state reaction method to sinter cubic phase LLZO samples with an ionic conductivity of 3.6×10^{-4} S cm^{-1} at 1230 °C. Lee et al. [7] achieved cubic phase LLZO by doping aluminum and obtained an ionic conductivity of 4.9×10^{-4} S cm^{-1} at 25 °C with a sintering temperature of 1125 °C. The above research indicates that the sintering temperature, rather than other parameters, plays a key role in controlling "lithium loss." In fact, to achieve higher sintering rates, lower sintering temperatures, and improved electrochemical performance, researchers have explored many unconventional sintering methods for the preparation of solid electrolytes [23–27]. Kotobuki et al. [23] utilized SPS sintering technology to reduce the grain boundaries of Y-doped LLZO, resulting in a sample prepared at 1100 °C with a relative density of 99.7% and an ionic conductivity of 9.8×10^{-4} S cm^{-1}. Yamada et al. [25] prepared Ta-doped LLZO with a relative density of 95.5% using SPS technology at 1000 °C for 10 min, achieving an ionic conductivity of 6.9×10^{-4} S cm^{-1} at 25 °C. Lu et al. [26] prepared aluminum-doped LLZO using microwave sintering at 1150 °C for 30 min, resulting in an ionic conductivity of 1.15×10^{-4} S cm^{-1}. With the emergence of FS technology, a multitude of ceramic materials have undergone sintering via this method [28–32]. FS technology, known for its ability to operate at lower temperatures and achieve swift densification, is suitable for the sintering of LLZO materials, which helps significantly in diminishing lithium evaporation. By using flash sintering to manufacture LLZO electrolytes, the significant lithium volatilization that occurs during long periods at high temperatures can be obviously reduced.

This study systematically investigates $Li_{7-x}La_3Zr_{2-x}Ta_xO_{12}$ (LLZTO, $x = 0.2$, 0.4, 0.6, and 0.8) to explore the effects of Ta doping on its structure and electrochemical properties. LLZTO samples with varying Ta doping concentrations were successfully prepared using flash sintering at 700 °C. Additionally, a full lithium cell was assembled using the Ta-LLZO solid electrolyte with optimized Ta content, and the cycle performance of the battery was studied.

Materials and methods

Preparation of Ta-doped $Li_{7-x}La_3Zr_{2-x}Ta_xO_{12}$ ($x = 0.2$, 0.4, 0.6, 0.8) solid electrolytes

$Li_{7-x}La_3Zr_{2-x}Ta_xO_{12}$ ($x = 0.2$, 0.4, 0.6, 0.8) solid electrolyte was synthesized in this experiment. The process involved

two steps: powder synthesis using the solid-state reaction method and sintering of the electrolyte ceramic sheets using the flash sintering technique.

Powder preparation of Ta-doped LLZO

The experiments were carried out with a commercial powder; LiOH·H$_2$O (Aladdin, 99.5 wt%), La$_2$O$_3$ (Aladdin, 99.99 wt%), ZrO$_2$ (Aladdin, 99.99 wt%), and Ta$_2$O$_5$ (Aladdin, 99.5 wt%) were used as starting reactants. The chemicals were weighed in accordance with the stoichiometric ratio. The mixed powders were ball-milled in a planetary ball mill at a speed of 400 r/min for 12 h, using isopropanol as the solvent, with a powder-to-ball ratio of 3:1. The ball-milled samples were dried at 80 °C for 12 h. The dried powder was then heated to 900 °C at 5 °C min^{-1} and calcined for 6 h.

Preparation of Ta-LLZO electrolyte by flash sintering

The as-received powders were uniaxially cold-pressed at 3 MPa to form cylinders with a diameter of 10 mm. Subsequently, sintering was carried out in the modified hot pressing furnace (Nanjing Boyuntong Instrument Technology Co., Ltd., RYL1700). For the flash sintering process of LLZTO, the compacted powder was placed in the modified hot pressing furnace, which was under vacuum. The powder was heated at a rate of 10 °C/min to 700 °C under the condition of constant pressure of 70 Pa. The temperature was held at 700 °C for 10 min until the internal temperature stabilized. An alternating current power supply (ZGYSH-6100; 30 A, 300 V, 9 KW) was used to apply electric field strength of 90 V/cm, current density of 380 mA/mm^2, and frequency of 400 Hz to the sample. After 15 min of continuous current supply, the power was disconnected, and the heating was stopped. The sample was allowed to cool to room temperature within the furnace before removal.

Preparation of battery

LLZO doped with 0.6 mol Ta was selected for the full lithium battery. The sintered LLZTO ceramic was polished and buffed on both sides using sandpaper, and then it was placed in a glove box filled with argon gas. Use LiFePO$_4$ as the cathode material and lithium metal foil as the anode material for the lithium battery.

The method for preparing the LiFePO$_4$ (LFP) cathode sheet was as follows: LFP powder, Super P, and PVDF (polyvinylidene difluoride) were weighed in a mass ratio of 8:1:1, mixed, and ground with N-methyl-2-pyrrolidone (NMP) to obtain a slurry. The slurry was applied evenly onto aluminum foil, then dried in a 60 °C oven for 12 h. After drying, it was cut into circular electrode sheets with a diameter of 6 mm, and

the loading of the active material was controlled at 1.2–1.6 mg cm^{-2}.

Lithium metal solid-state battery (LMSSB), a 2032 coin cell was assembled using the prepared Ta-LLZO solid electrolyte (referred to as Li/LLZTO/LFP) in a glove box filled with argon atmosphere (O$_2$ < 0.1 ppm, H$_2$O < 0.1 ppm), LFP served as the cathode, and lithium metal was used as the anode. To improve interfacial contact, 5 μL LiPF$_6$ liquid electrolyte was used to wet the interface between LLZTO and LFP. Li‖Li symmetric cells were assembled by the same method.

Characterization

The LLZTO prepared by flash sintering was characterized using X-ray diffraction (XRD, D/max-2500PC, Japan) to confirm the sample's phase structure. Scanning electron microscopy (SEM, S4800, Japan) was employed to observe the microstructure and characteristics of the sample surface, while energy-dispersive X-ray spectroscopy (EDS) (Oxford Instrument X-MAX50mm2SDD) was used to analyze the element distribution and composition of the sample. X-ray photoelectron spectroscopy (XPS) system (Thermo Fisher Scientific, USA) was utilized to determine the valence states of tantalum doping elements in the solid electrolyte samples and the air stability of the sintered samples. The density of the sintered samples was measured using the Archimedes method. Raman spectroscopy (RTS-EX, TEO) was used to determine the crystal structure and perform quantitative analysis of all samples through their molecular vibrations. The testing wavelength range was set from 100 to 1200 cm^{-1}, with a laser wavelength of 532 nm.

At room temperature, impedance measurements were conducted using an electrochemical analyzer (Shanghai Chenhua, CHI660E) with a frequency range of 0.1 Hz to 1 MHz and an AC amplitude of 5 mV. Prior to testing, both sides of the LLZTO sample were polished and coated with a layer of silver paste, followed by drying at 80 °C to obtain an Ag/LLZTO/Ag symmetrical cell. The formula for calculating the ion conductivity is as follows:

$$\sigma = \frac{d}{AR} \tag{1}$$

where σ, d, A, and R represent the conductivity, the thickness of the sample, the area of the Ag electrode, and the resistance. Apply a 5 V voltage to the ceramic sample sheet to measure the time–current curve of the ammeter. The contribution of the sample's electronic conductivity to the total conductivity is calculated using the following equation:

$$\sigma = \frac{LI_{\text{final}}}{US} \tag{2}$$

where L, I_{final}, U, and S represent the sample thickness, steady-state current, test voltage, and area, respectively.

The coin cell (2032-type) assembled with Li$_{6.4}$La$_3$Zr$_{1.4}$Ta$_{0.6}$O$_{12}$ as the electrolyte was tested for battery performance at 50 °C. Impedance measurements were conducted on a Li/LLZTO/Li symmetric cell using an electrochemical analyzer (Shanghai Chenhua, CHI660E) with a frequency range of 0.01 Hz to 1 MHz and an AC amplitude of 5 mV. The critical current density and Li stripping/deposition tests were performed on the Li/LLZTO/Li symmetric cell using a battery measurement system (LK2005A, Shanghai Kejing Zhida Technology Co, Ltd., China). Additionally, charge–discharge cycle tests and rate tests were carried out on the Li/LLZTO/LFP battery.

Results and discussion

The variation of the electric field, current density, and power density of LLZTO (Ta 0.2–0.8) composites with time during flash sintering is shown in Fig. 1. The results showed that the actual electric fields in FS of samples with different Ta doping amount are different. With the increase of Ta doping, the threshold electric field decreases, which indicates that Ta doping is beneficial to FS. When the doping amount of Ta is 0.6, the threshold electric field reached the lowest value. Therefore, the most direct reason for Ta dopant affecting FS behavior is that the increase of Ta doping leads to an increase in the initial conductivity of FS samples, making the FS easier to occur. As discussed in our previous paper [33, 34], the flash sintering process is mainly divided into three stages. The main densification process of the sample is completed within a few seconds, accompanied by the phenomenon of electroluminescence in stage II. From Fig. 1c, it can be seen that the electric field decreased slightly, while the current density increased to the maximum level in this process, both electric parameters remained at the higher value, implying the higher relative density under the present condition.

Based on the above discussion, to understand the sintering behavior and substituted process of the Ta-doped LLZO, the schematic diagram of the sintering processing was depicted in Fig. 1e. From the beginning of stage I, Joule heating, and thermal runaway, accordingly, the surrounding temperature and the conductivity increased [35–37]. Once the current reached to the pre-set value, or even exceeded, the power mode was converted from voltage control to current control instantaneously. At this time, the shrinkage of the sample observed in the FS process corresponds to the lattice constant size change of LLZTO resulting in the distortion of the lattice structure.

The calculated lattice parameters are shown in Table 1. From the results, lattice parameters decreased slightly
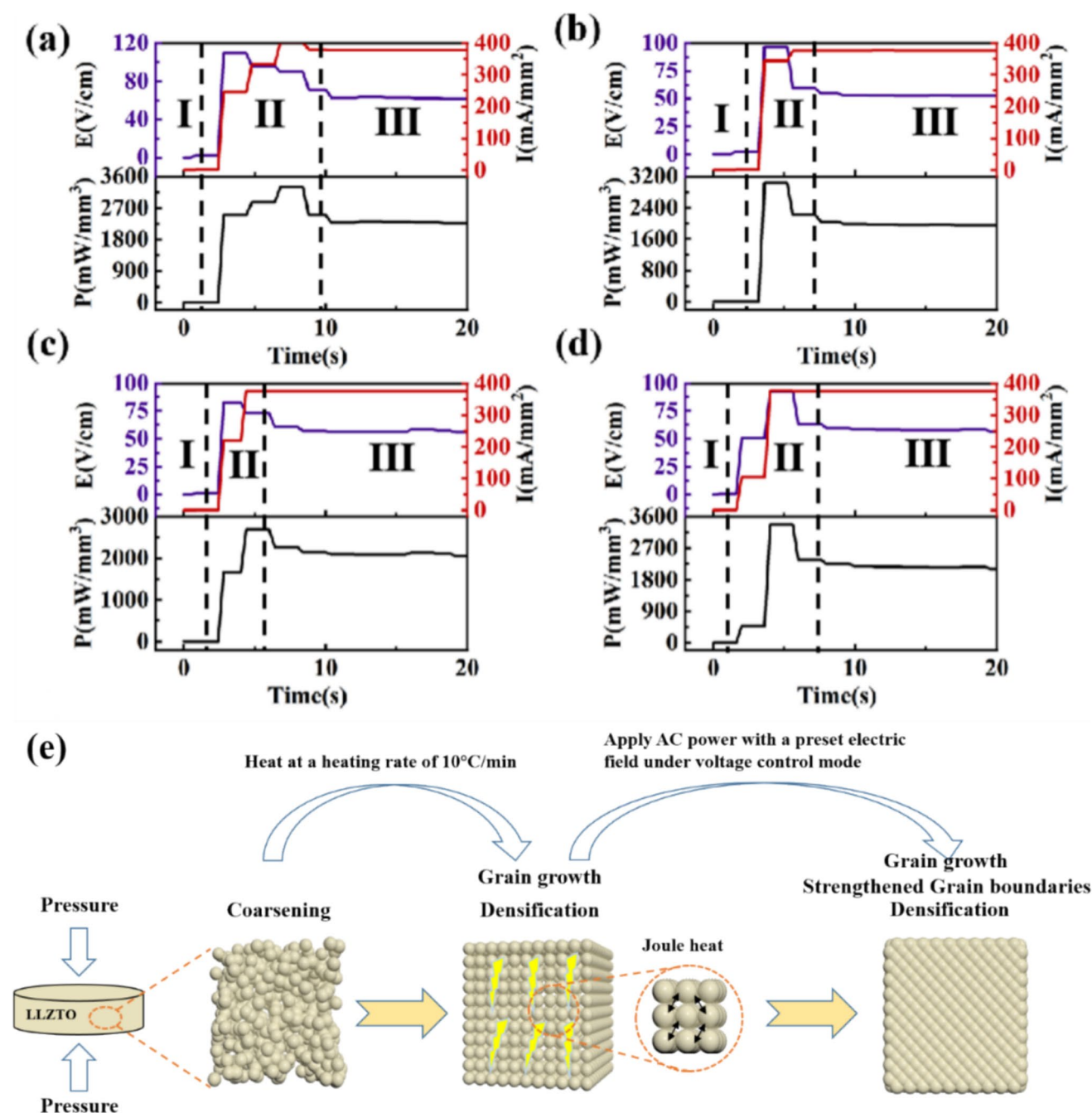
Fig. 1 Flash sintering curves of LLZTO electrolyte with different Ta^{5+} contents: **a** 0.2, **b** 0.4, **c** 0.6, **d** 0.8; **e** schematic diagram of LLZTO sintering process

with the increasing of Ta^{5+} doping content, and the minimum is 12.8597 Å at $Li_{6.4}La_3Zr_{1.4}Ta_{0.6}O_{12}$ because Ta^{5+} (0.68 Å) is slightly smaller than Zr^{4+} (0.72 Å). The substitution of high-valence Ta^{5+} with a small atomic radius will not occupy the channel sites of the Li^+ network, but it will reduce the content of Li^+ and increase the concentration of lithium vacancy. At the same time, theoretically, it will cause the reduction of cell size, resulting in

lattice distortion, expanding the carrier channel size, and improving the transport performance of lithium ions. The performances of Ta-doped LLZO, including relative density and Li-ion conductivity, are affected by Li vacancy concentration. The functions of Li vacancy concentration for Ta-doped LLZO mainly consist of stabilizing c-LLZO, densification process of ceramic, and therefore effects for cycling stability of assembled SSLBs. Overall, the effects

Table 1 The ionic conductivity, relative density, phase structure, lattice parameter (Å) electron conductivity, and estimated sintering temperature of $Li_{7-x}La_3Zr_{2-x}Ta_xO_{12}$ ($x=0.2,0.4,0.6,0.8$)

	$x=0.2$	$x=0.4$	$x=0.6$	$x=0.8$
σ_{total} (S cm^{-1})	5.0×10^{-5}	1.2×10^{-4}	9.8×10^{-4}	7.5×10^{-4}
Relative density (%)	90.84	93.16	94.72	92.2
Phase (s)	Cubic, tetragonal	Cubic	Cubic	Cubic, tetragonal
Lattice parameter (Å)	12.9916	12.9910	12.8597	12.9093
σ_e (S cm^{-1})	5.66×10^{-10}	3.58×10^{-8}	4.23×10^{-8}	6.4×10^{-9}
Estimated sintering temperature (°C)	2610	2560	2500	2580

of Ta^{5+} content on the crystal structure of the doped composites were proved in the following parts.

As reported, the actual temperature of samples under flash sintering is much higher than the furnace temperature due to Joule heating. It could be estimated according to the blackbody radiation model (BBR) established in the literature [38]. The actual internal temperature of the sintered composites shown in Table 1 reaches above 2400 °C, which is adequate to occur the liquid sintering even though the low furnace temperature is 700 °C. During the sintering process, the addition of Ta^{5+} formed the electronic conduction of the composite and promoted sintering which would lead to further densification [39, 40]. The resulting relative density of $Li_{7-x}La_3Zr_{2-x}Ta_xO_{12}$ ($0.2\leq x\leq 0.8$) obtained by the Archimedean drainage method is shown in Table 1. With the increase of doping content, the relative density also increases, reaching a maximum of 94.72% when the Ta content is 0.6 mol. Comparison with our previous work (Fig. S1 and Table S1) suggests that appropriate doping can enhance the densification process during sintering.

The flash-sintered specimens were further characterized by X-ray diffraction (XRD) and scanning electron microscopy (SEM). As can be seen from Fig. 2, the sintered composite appears incomplete cubic phase transition when Ta^{5+} doping content is 0.2 mol. Further increasing the doping amount can form a stable pure cubic phase structure. The sample with a Ta^{5+} doping content of $x=0.4$ can form a relatively stable cubic phase structure, but its diffraction peak intensity is low, indicating insufficient crystallinity of the sample. When the Ta^{5+} doping content is increased to $x=0.6$, a stable cubic phase structure is formed, and the diffraction peak intensity is significantly enhanced, indicating good crystallinity. When Ta content increased to 0.8 mol, some diffraction peaks appeared implying cubic phases changing into tetragonal phase structure, and simultaneously, a small amount of impurities are formed.

Figure 3 shows the SEM micrograph of a fracture surface which is consistent with very low porosity in the specimen, expected from its high relative density. The fracture morphology is seen to be transgranular, which implies strong cohesion at grain boundaries. We compared the results with the powder grain before sintering (Fig. S2),
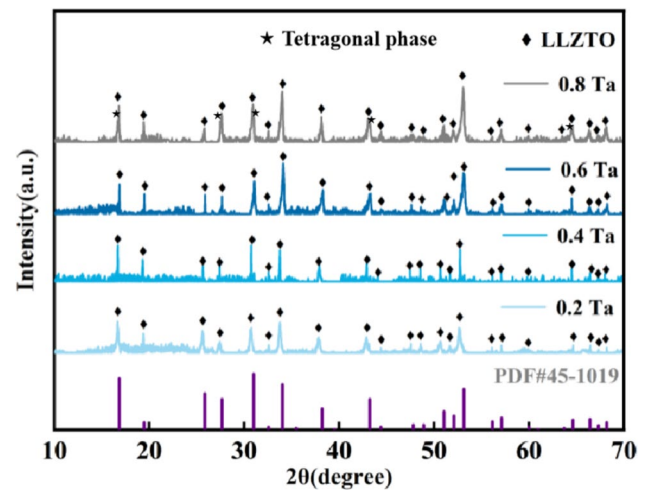

Fig. 2 XRD patterns of $Li_{7-x}La_3Zr_{2-x}Ta_xO_{12}$ ($0.2\leq x\leq 0.8$) with different Ta^{5+} doping contents

the grain size range increased from 1–5 μm before sintering to 2–18 μm after sintering. The medium grain size grew from 1.5–3 μm to 5–8 μm. Combined with the above results, it is verified that an appropriate amount of Ta^{5+} doping can stabilize the cubic crystal structure. As the Ta dopant reaches 0.6, the grains grow to be larger. It contributes to the highest value of the relative density, which is attributed to the optimal Li vacancies concentration. The EDS element mapping at a doping content of $x=0.6$, as shown in Fig. 3i, reveals the uniform distribution of elements within the particles, demonstrating the successful introduction of the Ta dopant.

We performed Raman spectroscopy on LLZO samples with different Ta doping levels. The obtained Raman spectra are shown in Fig. 4. According to the literature [41], the vibration peak of La^{3+} in LLZO corresponds to the range of 100–150 cm^{-1}. The vibration peaks of the LiO$_6$ octahedra and LiO$_4$ tetrahedra are located in the ranges of 200–300 cm^{-1} and 350–500 cm^{-1}, respectively. The Raman peak around 640 cm^{-1} corresponds to the vibration mode of the Zr-O bond, which is similar to the vibration mode reported for Ta-doped LLZO in the literature [42]. The Raman peaks observed at 215, 260, 360, 410, 515, and
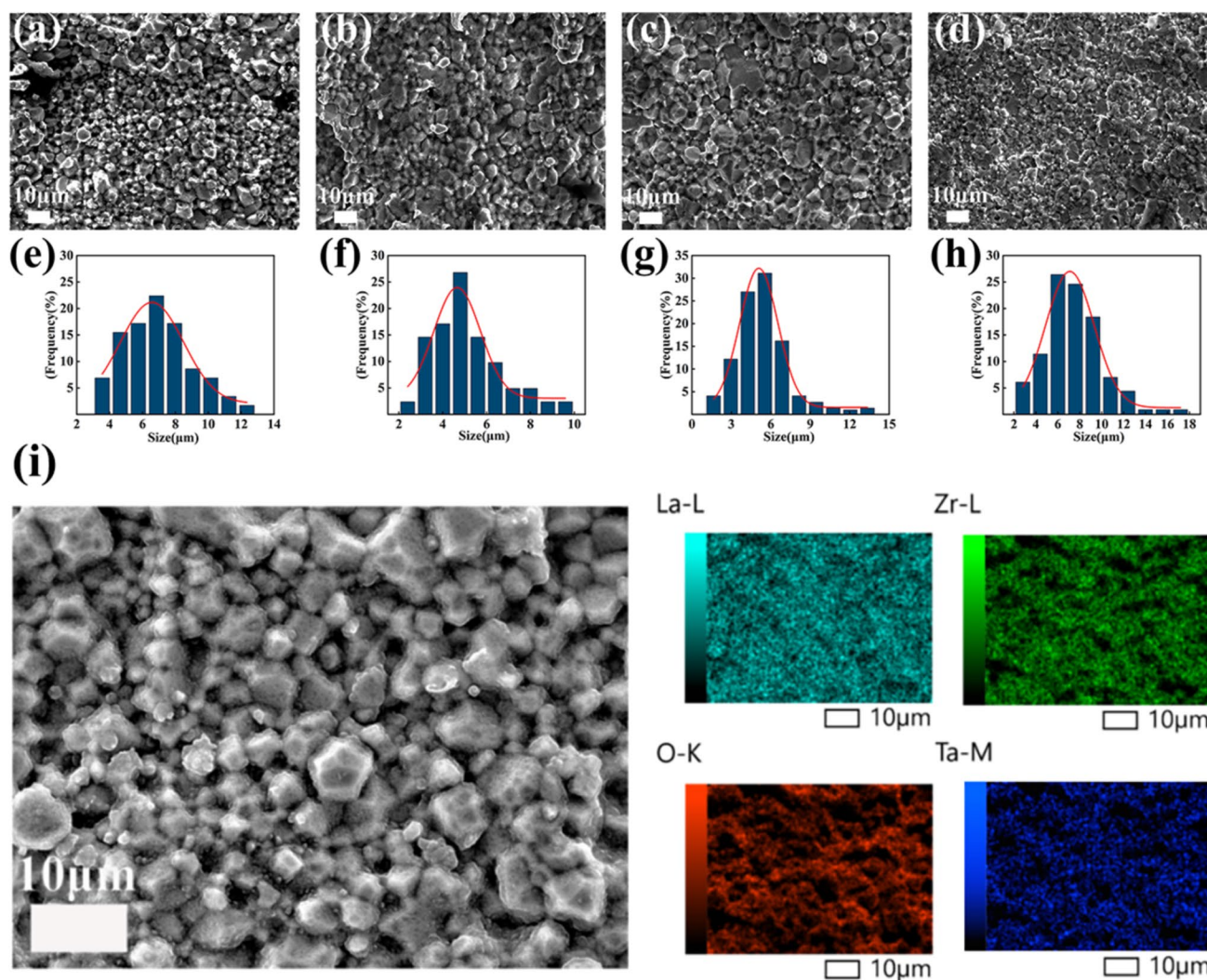
Fig. 3 **a–h** Fracture morphology and corresponding size distribution of $Li_{7-x}La_3Zr_{2-x}Ta_xO_{12}$ ($0.2 \leq x \leq 0.8$) sample, **i** energy spectrum of $Li_{6.4}La_3Zr_{1.4}Ta_{0.6}O_{12}$ sample.
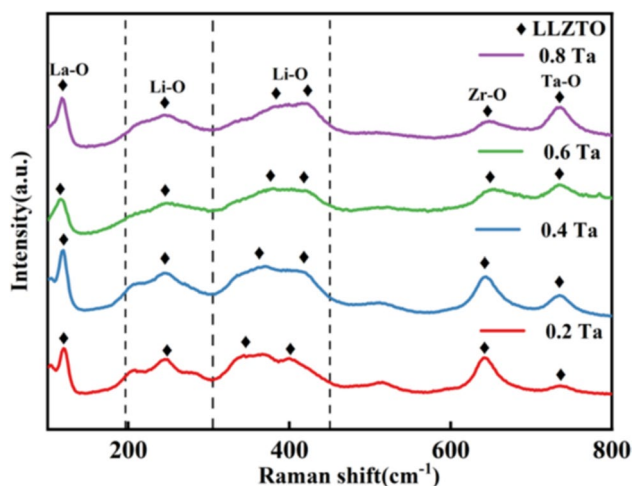
Fig. 4 Raman spectra of the sintered samples $Li_{7-x}La_3Zr_{2-x}Ta_xO_{12}$ ($0.2 \leq x \leq 0.8$)

650 cm^{-1} in the figure can be used as markers to identify the cubic phase of the LLZO structure.

To further investigate the effect of Ta^{5+} doping on the surface stability of the material, X-ray photoelectron spectroscopy (XPS) analysis was conducted. Typically, Li_2CO_3 impurities lead to an increase in the ionic resistance of sintered composite materials. As shown in Fig. 5, the surface elemental composition of the Ta0.6-LLZO and the pristine LLZO electrolytes was analyzed. The O1s signal at 531.6 eV binding energy and the Li1s signal at 55.5 eV binding energy are associated with Li_2CO_3. By comparing the samples before and after doping, it was found that the peak areas at 531.6 eV and 55.5 eV for Ta0.6-LLZO were smaller than those of the pristine sample. The results indicate that Ta^{5+} doping contributes to the stability of the cubic structure.

The corresponding Nyquist diagram of LLZTO solid electrolytes with different Ta content measured at room

Fig. 5 XPS spectra of a sintered sample of **a**–**c** LLZO, **d**–**f** $Li_{7-x}La_3Zr_{2-x}Ta_xO_{12}$ ($x=0.6$)
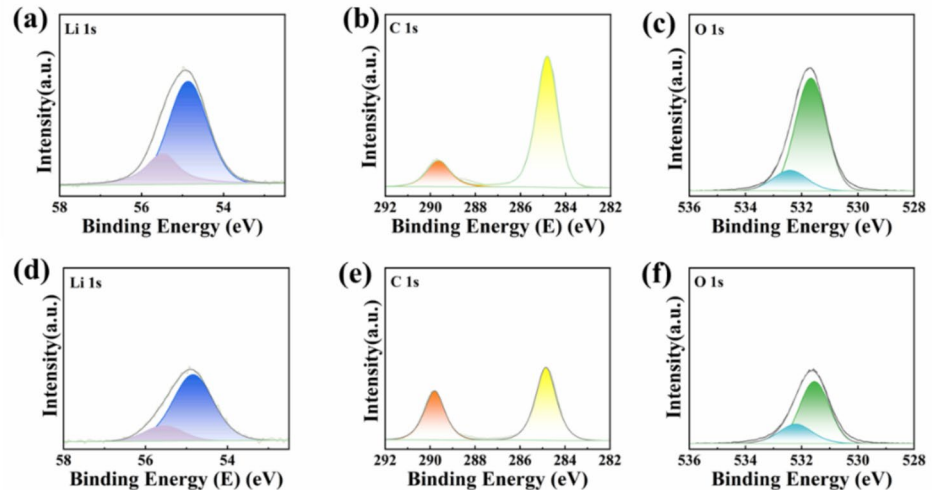
temperature was shown in Fig. 6a. The total lithium-ion conductivity measured with impedance spectroscopy at room temperature was shown in Table 1, significantly higher than the values reported in the literature with the conventional or hot pressing techniques [43, 44]. Compared with existing work (Fig. S3, Table S1, and Table S2), better ionic conductivity can be achieved at lower furnace temperatures and in a shorter time. The maximum ionic conductivity was obtained when the doping amount of Ta^{5+} was 0.6 mol. While the amount of Ta^{5+} increased to 0.8 mol, the impurity phase with a tetragonal structure and poor conductivity appeared, and the low carrier concentration resulting in the decrease of conductivity. The direct current polarization (i-t) curves of electrolyte sheets with different amounts of Ta^{5+} doping were tested at room temperature, as shown in Fig. 6b, to characterize the electronic conductivity of the electrolyte sheets. The specific electronic conductivity values were calculated using formula (2) and are presented in Table 1. The electronic conductivities are more than four orders of magnitude lower than the ionic conductivities and are not significantly affected by the doping amount or sintering process, confirming that the electrolyte primarily conductions.

The ability of Ta-LLZO to suppress lithium dendrites was investigated by assembling lithium symmetric cells. The impedance of the tested Li/LLZTO/Li symmetric cell is shown in Fig. 7a. The Nyquist plot of the Li/LLZTO/Li symmetric cell displays a semicircle, attributed to the Li/LLZTO interface, with the starting point of the semicircle corresponding to the bulk resistance of LLZTO. The Li/LLZTO/Li symmetric cell was charged and discharged at a current density of 0.1 mA cm^{-2} for 0.5 h at 50 °C. The results are shown in Fig. 7b. The Li/LLZTO/Li cell was able to operate continuously for over 200 h without a short circuit and without any voltage drops, demonstrating its effective capability to suppress lithium dendrites. The critical current density (CCD) test reflects the tolerance of the electrolyte LLZTO and the Li/LLZTO interface to lithium dendrite growth at high current densities. This was conducted by performing constant current charge–discharge tests on lithium symmetric cells, with the current density increased in steps of 0.1 mA cm^{-2} starting from 0.1 up to 0.7 mA cm^{-2}. Each charge/discharge cycle was maintained for 1 h. As shown in Fig. 7c, the red solid line represents the voltage curve. The results show that at a current density of 0.7 mA cm^{-2},

Fig. 6 **a** Typical impedance spectra and equivalent circuits of Ag/LLZTO/Ag particles with different Ta^{5+} doping amounts and **b** DC polarization curves of Ag/LLZTO/Ag samples at 25 °C and 5.0 V.
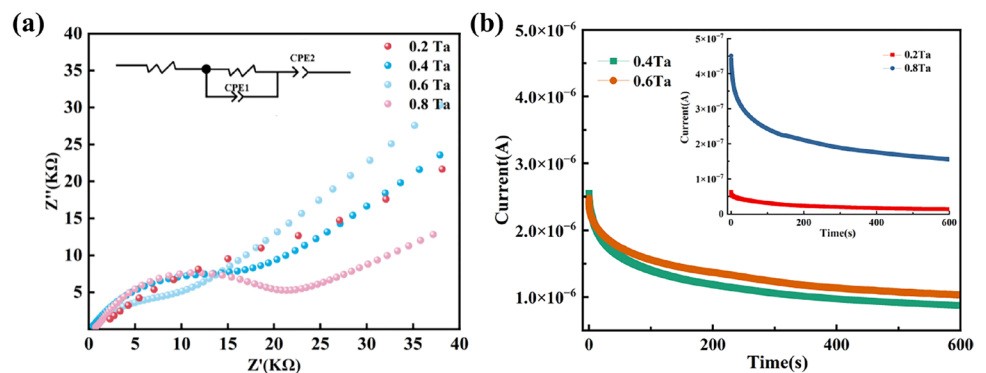
Fig. 7 Electrochemical performance of Li/LLZTO/Li symmetric battery and Li/LLZTO/LFP battery at 50 °C. **a** EIS curve of Li/LLZTO/Li symmetric battery. **b** Galvanostatic cycling curves of Li/LLZTO/Li symmetric cells 0.1 mA cm^{-2}. **c** Critical current density test of Li/LLZTO/Li symmetric battery. **d** Cycling stability of Li/LLZTO/LFP battery at 0.1C rate. **e** Discharge and charge voltage profiles at 0.1C. **f** Rate performance of Li/LLZTO/LFP battery at different rates. **g** Galvanostatic charge and discharge profiles of Li/LLZTO/LFP battery at different rates
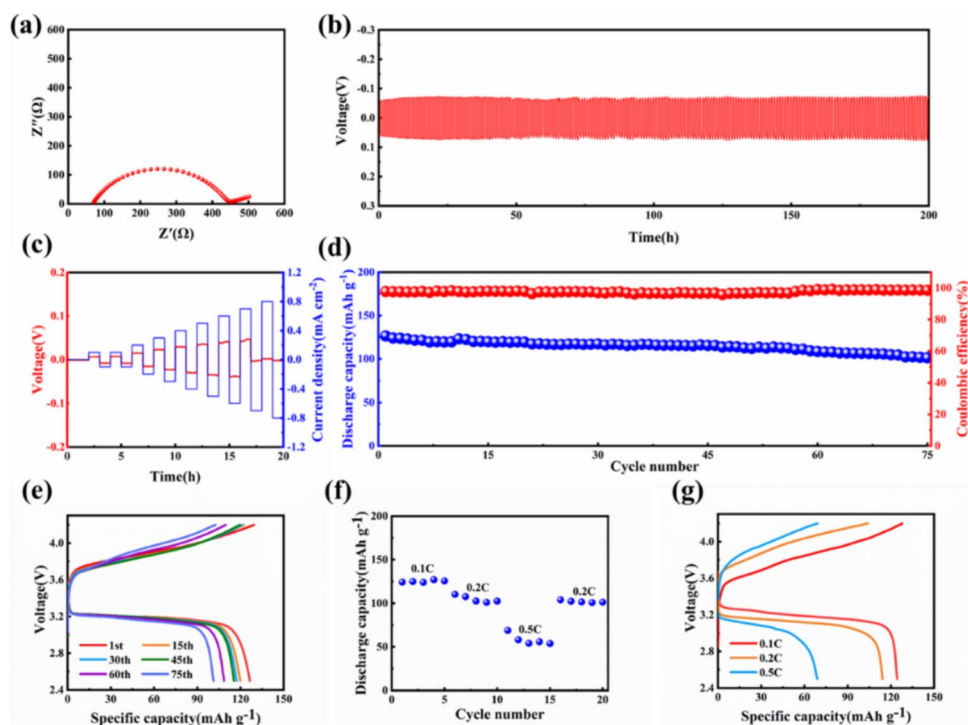
there was a sudden change in voltage, indicating that during this process, the interface first experienced excessive polarization, leading to partial contact failure, followed by a phenomenon of locally high current density, which induced lithium dendrite growth and resulted in internal short-circuiting. Therefore, the limiting current of the cell is approximately 0.7 mA cm^{-2}. Compared to existing work (Table S3), the results show that a higher CCD can effectively suppress the formation of lithium dendrites.

The electrochemical properties of Li/LLZTO/LFP were tested using a blue electric battery testing system. The 0.1C test at 50 °C was conducted to investigate its cycling performance and capacity retention. The charge–discharge curves of Li/LLZTO/LFP are shown in Fig. 7d, e. As shown in Fig. 7d, the first discharge specific capacity of Li/LLZTO/LFP is 126.5 mAh g^{-1}. After 75 cycles, the discharge capacity decreases to 101.3 mAh g^{-1}, and the corresponding capacity retention rate is 79%. Rate performance tests for Li/ LLZTO/LFP batteries at different current densities ranging from 0.1C to 0.5C were conducted, as shown in Fig. 7f, g. The specific capacities at 0.1C, 0.2C, and 0.5C were 124.3, 114.2, and 68.9 mAh g^{-1}, respectively. The capacity recovered to 104 mAh g^{-1} when the rate returned to 0.2C. The specific capacity of the battery remains equivalent to the initial stage, indicating that the electrolyte possesses good reversibility.

Conclusions

The high-dense Ta-LLZO solid electrolyte was successfully synthesized at 700 °C by flash sintering technology. The effect of Ta doping content on the microstructure and electrochemical performance of LLZTO was investigated. Furthermore, XPS tests were conducted on the surface of LLZO and Ta0.6-LLZO, and the results indicate that the surface of the Ta0.6-LLZO is phase stable. When the Ta doping content was 0.6 mol, the ionic conductivity could reach 9.8×10^{-4} S cm^{-1}. An initial discharge specific capacity of 126.5 mAh g^{-1} under 0.1C rate at 50 °C for the assembled Li/LLZTO/LFP solid-state lithium metal battery was obtained.

Data availability Data is provided within the manuscript or supplementary information files.

Declarations

Ethical approval Not applicable.

Competing interests The authors declare no competing interests.

References

1. Zhang JG, Xu W, Xiao J, Cao X, Liu J (2020) Lithium metal anodes with nonaqueous electrolytes. Chem Rev 120:13312. https://doi.org/10.1021/acs.chemrev.0c00275

2. Xia S, Wu X, Zhang Z, Cui Y, Liu W (2019) Practical challenges and future perspectives of all-solid-state lithium-metal batteries. Chem 5:753. https://doi.org/10.1016/j.chempr.2018.11.013

3. Zheng C, Lu Y, Su J et al (2022) Grain boundary engineering enabled high-performance garnet-type electrolyte for lithium dendrite free lithium metal batteries. Small Methods 6:e2200667. https://doi.org/10.1002/smtd.202200667

4. Vishnugopi BS, Kazyak E, Lewis JA et al (2021) Challenges and opportunities for fast charging of solid-state lithium metal batteries. ACS Energy Lett 6:3734. https://doi.org/10.1021/acsenergylett.1c01352

5. Liu G, Shi J, Zhu M et al (2021) Ultra-thin free-standing sulfide solid electrolyte film for cell-level high energy density all-solid-state lithium batteries. Energy Storage Materials 38:249. https://doi.org/10.1016/j.ensm.2021.03.017

6. Hu T, Shen X, Peng L, et al (2021) Preparation of single-ion conductor solid polymer electrolyte by multi-nozzle electrospinning process for lithium-ion batteries. J Phys Chem Solids 158. https://doi.org/10.1016/j.jpcs.2021.110229

7. Lee J-M, Kim T, Baek S-W et al (2014) High lithium ion conductivity of Li7La3Zr2O12 synthesized by solid state reaction. Solid State Ionics 258:13. https://doi.org/10.1016/j.ssi.2014.01.043

8. Murugan R, Thangadurai V, Weppner W (2007) Fast lithium ion conduction in garnet-type Li(7)La(3)Zr(2)O(12). Angew Chem Int Ed Engl 46:7778. https://doi.org/10.1002/anie.200701144

9. Ohta S, Kobayashi T, Asaoka T (2011) High lithium ionic conductivity in the garnet-type oxide Li7−X La3(Zr2−X, NbX)O12 (X=0–2). J Power Sources 196:3342. https://doi.org/10.1016/j.jpowsour.2010.11.089

10. Sastre J, Priebe A, Döbeli M, Michler J, Tiwari AN , Romanyuk YE (2020) Lithium garnet Li7La3Zr2O12 electrolyte for all-solid-state batteries: closing the gap between bulk and thin film Li-ion conductivities. Advanced Materials Interfaces 7. https://doi.org/10.1002/admi.202000425

11. Awaka J, Kijima N, Hayakawa H, Akimoto J (2009) Synthesis and structure analysis of tetragonal Li7La3Zr2O12 with the garnet-related type structure. J Solid State Chem 182:2046. https://doi.org/10.1016/j.jssc.2009.05.020

12. Awaka J, Takashima A, Kataoka K, Kijima N, Idemoto Y, Akimoto J (2011) Crystal structure of fast lithium-ion-conducting cubic Li7La3Zr2O12. Chem Lett 40:60. https://doi.org/10.1246/cl.2011.60

13. Li Y, Wang Z, Cao Y et al (2015) W-doped Li7La3Zr2O12 ceramic electrolytes for solid state Li-ion batteries. Electrochim Acta 180:37. https://doi.org/10.1016/j.electacta.2015.08.046

14. Mishra M, Hsu C-W, Chandra Rath P, et al. (2020) Ga-doped lithium lanthanum zirconium oxide electrolyte for solid-state Li batteries. Electrochimica Acta 353. https://doi.org/10.1016/j.electacta.2020.136536

15. Song S, Chen B, Ruan Y et al (2018) Gd-doped Li7La3Zr2O12 garnet-type solid electrolytes for all-solid-state Li-ion batteries. Electrochim Acta 270:501. https://doi.org/10.1016/j.electacta.2018.03.101

16. Badami P, Weller JM, Wahab A et al (2020) Highly conductive garnet-type electrolytes: access to Li(6.5)La(3)Zr(1.5)Ta(0.5)O(12) prepared by molten salt and solid-state methods. ACS Appl Mater Interfaces 12: 48580. https://doi.org/10.1021/acsami.0c14056

17. Inada R, Takeda A, Yamazaki Y, Miyake S, Sakurai Y, Thangadurai V (2020) Effect of postannealing on the properties of a Ta-doped Li7La3Zr2O12 solid electrolyte degraded by Li dendrite penetration. ACS Applied Energy Materials 3:12517. https://doi.org/10.1021/acsaem.0c02474

18. Zhang Y, Deng J, Hu D et al (2019) Synergistic regulation of garnet-type Ta-doped Li7La3Zr2O12 solid electrolyte by Li+ concentration and Li+ transport channel size. Electrochim Acta 296:823. https://doi.org/10.1016/j.electacta.2018.11.136

19. Inada R, Kusakabe K, Tanaka T, Kudo S, Sakurai Y (2014) Synthesis and properties of Al-free Li7−xLa3Zr2−xTaxO12 garnet related oxides. Solid State Ionics 262:568. https://doi.org/10.1016/j.ssi.2013.09.008

20. Gong Y, Liu Z-G, Jin Y-J, Ouyang J-H, Chen L, Wang Y-J (2019) Effect of sintering process on the microstructure and ionic conductivity of Li7–La3Zr2–Ta O12 ceramics. Ceram Int 45:18439. https://doi.org/10.1016/j.ceramint.2019.06.061

21. Buschmann H, Berendts S, Mogwitz B, Janek J (2012) Lithium metal electrode kinetics and ionic conductivity of the solid lithium ion conductors "Li7La3Zr2O12" and Li7−La3Zr2−Ta O12 with garnet-type structure. J Power Sources 206:236. https://doi.org/10.1016/j.jpowsour.2012.01.094

22. Huang X, Xiu T, Badding ME, Wen Z (2018) Two-step sintering strategy to prepare dense Li-garnet electrolyte ceramics with high Li+ conductivity. Ceram Int 44:5660. https://doi.org/10.1016/j.ceramint.2017.12.217

23. Kotobuki M, Koishi M (2020) High conductive Al-free Y-doped Li7La3Zr2O12 prepared by spark plasma sintering. J Alloys Compd 826. https://doi.org/10.1016/j.jallcom.2020.154213

24. Yamada H, Ito T, HongahallyBasappa R, Bekarevich R, Mitsuishi K (2017) Influence of strain on local structure and lithium ionic conduction in garnet-type solid electrolyte. J Power Sources 368:97. https://doi.org/10.1016/j.jpowsour.2017.09.076

25. Yamada H, Ito T, HongahallyBasappa R (2016) Sintering mechanisms of high-performance garnet-type solid electrolyte densified by spark plasma sintering. Electrochim Acta 222:648. https://doi.org/10.1016/j.electacta.2016.11.020

26. Lu X, Yang D (2018) Preparation of garnet-type Li7 − 3xAlxLa3Zr2O12 at lower temperature by using powders of mixed pre-treatment conditions. J Inorg Organomet Polym Mater 28:2023. https://doi.org/10.1007/s10904-018-0859-y

27. Chen C, Wang K, He H, Hanc E, Kotobuki M, Lu L (2023) Processing and properties of garnet-type Li(7) La(3) Zr(2) O(12) ceramic electrolytes. Small 19:e2205550. https://doi.org/10.1002/smll.202205550

28. Shi R, Pu Y, Wang W et al (2019) Flash sintering of barium titanate. Ceram Int 45:7085. https://doi.org/10.1016/j.ceramint.2018.12.211

29. Biesuz M, Sglavo VM (2019) Flash sintering of ceramics. J Eur Ceram Soc 39:115. https://doi.org/10.1016/j.jeurceramsoc.2018.08.048

30. CEJ Dancer (2016) Flash sintering of ceramic materials. Materials Research Express 3. https://doi.org/10.1088/2053-1591/3/10/102001

31. Caliman LB, Bouchet R, Gouvea D, Soudant P, Steil MC (2016) Flash sintering of ionic conductors: the need of a reversible

electrochemical reaction. J Eur Ceram Soc 36:1253. https://doi.org/10.1016/j.jeurceramsoc.2015.12.005

32. Zhang J, Zhao Y, Qiao J, Sun W, Sun K, Wang Z (2020) An easily controllable flash sintering process for densification of electrolyte for application in solid oxide fuel cells. Int J Hydrogen Energy 45:17824. https://doi.org/10.1016/j.ijhydene.2020.04.204

33. Yang Y, Ma T, Zhang Z (2023) Effect of Cu/Ta-codoping on the microstructure and conductivity of Li7La3Zr2O12 by flash sintering. J Mater Sci 58:18003. https://doi.org/10.1007/s10853-023-09090-2

34. Yang Y, Zhao P, Ma T (2022) Effect of current density on the densification of 3%mol yttria-stabilized zirconia/carbon nanotube by flash sintering. J Mater Sci: Mater Electron 33:19901. https://doi.org/10.1007/s10854-022-08809-2

35. Grimley CA, Prette ALG, Dickey EC (2019) Effect of boundary conditions on reduction during early stage flash sintering of YSZ. Acta Mater 174:271. https://doi.org/10.1016/j.actamat.2019.05.001

36. Todd RI, Zapata-Solvas E, Bonilla RS, Sneddon T, Wilshaw PR (2015) Electrical characteristics of flash sintering: thermal runaway of Joule heating. J Eur Ceram Soc 35:1865. https://doi.org/10.1016/j.jeurceramsoc.2014.12.022

37. Demirskyi D, Vasylkiv O (2017) Hot-spots generation, exaggerated grain growth and mechanical performance of silicon carbide bulks consolidated by flash spark plasma sintering. J Alloy Compd 691:466. https://doi.org/10.1016/j.jallcom.2016.08.234

38. Raj R (2012) Joule heating during flash-sintering. J Eur Ceram Soc 32:2293. https://doi.org/10.1016/j.jeurceramsoc.2012.02.030

39. Biesuz M, Pinter L, Saunders T et al (2018) Investigation of electrochemical, optical and thermal effects during flash sintering of 8YSZ. Materials (Basel) 11. https://doi.org/10.3390/ma11071214

40. Masó N, West AR (2015) Electronic conductivity in yttria-stabilized zirconia under a small dc bias. Chem Mater 27:1552. https://doi.org/10.1021/cm503957x

41. Larraz G, Orera A, Sanjuán ML (2013) Cubic phases of garnet-type Li7La3Zr2O12: the role of hydration. J Mater Chem A 1. https://doi.org/10.1039/c3ta11996c

42. Dhivya L, Murugan R (2014) Effect of simultaneous substitution of Y and Ta on the stabilization of cubic phase, microstructure, and Li(+) conductivity of Li7La3Zr2O12 lithium garnet. ACS Appl Mater Interfaces 6:17606. https://doi.org/10.1021/am503731h

43. Gai J, Zhao E, Ma F et al (2018) Improving the Li-ion conductivity and air stability of cubic Li7La3Zr2O12 by the co-doping of Nb, Y on the Zr site. J Eur Ceram Soc 38:1673. https://doi.org/10.1016/j.jeurceramsoc.2017.12.002

44. Rangasamy E, Wolfenstine J, Sakamoto J (2012) The role of Al and Li concentration on the formation of cubic garnet solid electrolyte of nominal composition Li7La3Zr2O12. Solid State Ionics 206:28. https://doi.org/10.1016/j.ssi.2011.10.022